Anisotropic Behavior of Atmospheric Disturbances in Coastal Areas for Satellite Radar Interferometry: Significance and Mitigation Strategy

Pardis Ghobeiti-Nasab[1], Sami Samiei-Esfahany[1*]
(1) School of Surveying and Geospatial Engineering, The University of Tehran, Iran - Ghobeyti.pardis@ut.ac.ir - s.samieiEsfahany@ut.ac.ir

Keywords: InSAR,Tropospheric Delay,Anisotropic Turbulence,Variogram Modeling,Coastal Regions,Atmospheric Corrections.

Abstract

Tropospheric phase delays pose significant challenges for accurate deformation measurement using Interferometric Synthetic Aperture Radar (InSAR), especially in coastal regions characterized by complex atmospheric dynamics. Conventional correction methods typically assume isotropy, overlooking directional variations in atmospheric turbulence. In this study, we systematically investigate the anisotropic behavior of tropospheric delays across diverse geodynamic regions of Iran, including coastal areas (Makran Coast, southern Zagros, central Alborz) and inland regions (South Khorasan), using empirical variogram analyses on more than 1,200 interferograms. Our results confirm pronounced anisotropy in coastal zones, attributable to complex topography and variable moisture distributions. Among tested variogram models (exponential, Gaussian, spherical), the exponential model consistently provided the best fit, reducing variogram modeling error (RMSE) by up to 56.8% compared to alternative approaches. Further evaluation using Least Squares Collocation (LSC) under varying observational scenarios revealed that anisotropic modeling substantially improves tropospheric corrections, notably achieving a 50% accuracy enhancement (up to 15 cm) in sparse or uneven sampling conditions typical of coastal environments. However, under dense, uniform sampling, anisotropic modeling showed minimal advantage. These findings underscore the critical importance of considering anisotropic atmospheric turbulence to enhance the precision and reliability of InSAR-derived geophysical measurements, particularly in challenging coastal settings.

1. Introduction

nterferometric Synthetic Aperture Radar (InSAR) is a powerful remote sensing technique for monitoring ground deformation with millimeter-level precision, large-scale coverage, and all-weather operability (Gabriel et al., 1989; Massonnet and Feigl, 1998; Li et al., 2022). However, its accuracy is often limited by tropospheric delays caused by spatiotemporal variations in pressure, temperature, and humidity (Hanssen, 1998; Fattahi and Amelung, 2015).

While advanced time-series methods such as Persistent Scatterer Interferometry (PSI) and Small Baseline Subset (SBAS) aim to mitigate atmospheric effects (Minh et al., 2022), such delays remain a major error source, particularly for slow deformation signals. A key limitation of most correction strategies is their reliance on isotropic assumptions, neglecting directional variability in atmospheric turbulence (Agram and Simons, 2015; Zhan et al., 2015).

Tropospheric delays have long been recognized as a major source of InSAR error (Gabriel et al., 1989; Hanssen, 1998). Various statistical methods, ranging from pair-wise logic and stacking (Massonnet et al., 1995; Sandwell and Price, 1998) to spatiotemporal filters (Schmidt and Bürgmann, 2005; Wei et al., 2010; Ferretti et al., 2001), have been proposed to suppress them, often assuming uncorrelated or spatially low-frequency noise.

External datasets such as GPS-derived zenith total delay (ZTD) (Onn and Zebker, 2006; Löfgren et al., 2010), MODIS/MERIS satellite products (Li et al., 2009), and numerical weather models like ERA5 (Jolivet et al., 2011; Yu et al., 2018) offer further correction potential. However, limitations such as sparse GPS coverage, coarse model resolution, and local atmospheric heterogeneity hinder their effectiveness (Kinoshita et al., 2013; Hu et al., 2022).

Although these models often assume isotropic turbulence, earlier works suggest directional dependence. Hanssen (1998) and Jónsson et al. (2002) demonstrated anisotropic behavior using variograms. Knospe and Jónsson (2010) proposed the Marten model, while Wei et al. (2019) showed that anisotropy coexists with isotropic components in turbulence.

This study addresses the following questions:

- To what extent does tropospheric turbulence exhibit anisotropy in coastal versus inland areas?
- Which statistical model best fits atmospheric anisotropy?
- How does incorporating anisotropy affect the accuracy of atmospheric correction in various sampling conditions?

This paper is structured as follows. Section 2 introduces the theoretical background, including the components of the interferometric phase, the physics of atmospheric delay, and the statistical modeling framework. Section 3 presents a detailed analysis of anisotropic behavior in tropospheric turbulence using empirical variograms across coastal and inland regions. Section 4 evaluates the effectiveness of anisotropic versus isotropic models in correcting atmospheric delays under different spatial sampling scenarios using Least Squares Collocation (LSC). Finally, Section 5 summarizes the key findings and offers practical recommendations for incorporating anisotropic modeling in InSAR atmospheric correction workflows.

* Corresponding author

2. Investigation of Atmospheric Anisotropic Behavior in Coastal Areas

2.1 Variogram

A widely used approach to characterize the spatial variability of atmospheric turbulence is through structure functions, commonly referred to as variograms (Hanssen, 2001; Wei et al., 2019). The one-dimensional variogram is defined as:

$$\gamma(r) = 1/2\ [(z(x_i) - z(x_i + r))^2] \qquad (1)$$

where z represents the observed sample at location x_i, and r is the spatial lag (distance). To investigate directional dependencies, along the north–south and east–west axes, the variogram is extended to a two-dimensional formulation:

$$\gamma(r_x, r_\gamma) = 1/2\ [(z(x, y) - z(x + r_x, y + r_\gamma))^2] \qquad (2)$$

where r_x and r_γ represent lags in the east–west and north–south directions, respectively.

Depending on the directional behavior of turbulence, the resulting variogram may exhibit either isotropic or anisotropic characteristics. In anisotropic cases, the variogram surface takes an elliptical form, indicating geometric anisotropy.

To model this anisotropy, theoretical variogram models were selected from the function sets presented by Goovaerts (1997), including exponential, Gaussian, and spherical models. These models ensure a positive-definite structure and are summarized in Table 1.

Name	Autocorrelation($Q(r)$)-Variogram Functions($\gamma(r)$)
Exponential	$Q(r) = \sigma^2 \left(e^{-d/r}\right)$ $\gamma(r) = \sigma^2 \left(1 - e^{-d/r}\right)$
Gaussian	$Q(r) = \sigma^2 \left(e^{-(d/r)^2}\right)$ $\gamma(r) = \sigma^2 \left(1 - e^{-(d/r)^2}\right)$
Spherical	$Q(r) = \sigma^2 \left(1 - \frac{3}{2}\frac{d}{r} + \frac{1}{2}\left(\frac{d}{r}\right)^3\right),\ d \le r$ $Q(r) = 0,\ d > r$ $\gamma(r) = \sigma^2 \left(\frac{3}{2}\frac{d}{r} - \frac{1}{2}\left(\frac{d}{r}\right)^3\right),\ d \le r$ $\gamma(r) = \sigma^2,\ d > r$

Table 1. Autocorrelation and variogram functions for spatial models.

In these functions, d denotes the spatial distance, and r is the correlation range. To incorporate geometric anisotropy, the distance ratio d/r is modified as follows:

$$\sqrt{\left(\frac{r_x \cos(\theta) + r_y \sin(\theta)}{a_{\max}}\right)^2 + \left(\frac{-r_x \sin(\theta) + r_y \cos(\theta)}{a_{\min}}\right)^2} \qquad (3)$$

Here, r_x and r_γ denote spatial lags in the east–west and north–south directions, θ is the azimuth angle of maximum continuity, and a_{max}, a_{min} represent the major and minor correlation ranges, respectively.
Following model fitting, the most compatible variogram (based on empirical behavior) will be used in the Least Squares Collocation (LSC) framework to predict atmospheric phase delays.

2.2 Study Areas and Data

To investigate the anisotropic behavior of the turbulent component of the troposphere, five study regions, both coastal and non-coastal, were analyzed. These include the Central Zagros (inland), Central Alborz (coastal), Southern Khorasan (inland), Southern Zagros (coastal), and the Western and Eastern Makran regions (coastal). The spatial distribution of these study areas is illustrated in Figure 1.

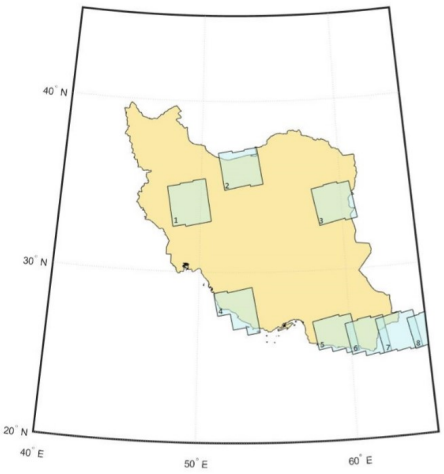

Figure 1. Study areas: 1. Middle Zagros (non-coastal), 2. Central Alborz (coastal), 3. South Khorasan (non-coastal), 4. South Zagros (coastal), 5. Western Makran (coastal), 6. Eastern Makran (coastal).

Among these regions, the Makran Coast has been designated as the primary study area due to its geodynamic complexity. Located at the boundary between the Arabian and Indian tectonic plates, this region is characterized by significant tectonic activity, necessitating precise atmospheric corrections to mitigate potential errors in interferometric analysis. The additional regions were selected to facilitate a comparative assessment of atmospheric behavior across distinct geological and climatic settings.
For this study, interferometric datasets were acquired from the School of Earth and Environment at the University of Leeds. The dataset comprises 1200 interferograms, spanning the period from 2014 to 2022, with temporal baselines ranging from 6 to 12 days. These interferograms provide a robust foundation for analyzing atmospheric variability in the selected study areas.
To correct for atmospheric phase turbulence, the interferograms were processed using the Geocoded Atmospheric Correction for Synthetic Aperture Radar (GACOS) service, which offers high-resolution tropospheric corrections. The necessary atmospheric correction data were systematically retrieved and applied to each interferogram, ensuring a reliable statistical analysis. The corrected interferometric phase was subsequently used for detailed interpretation and comparative evaluation of atmospheric effects across the selected regions.

2.3 Phase Decomposition

As previously mentioned, a short temporal baseline minimizes the deformation phase contribution ($\delta_{deformation}$), while a short spatial baseline reduces the impact of the flat Earth phase (δ_{Flat}). Additionally, the use of a high-resolution regional Digital

Elevation Model (DEM) improves the modeling and removal of the topographic phase ($\delta_{Topography}$). Consequently, the remaining interferometric phase can be expressed as:

$$\Psi_{ms} = \Psi_{atmo} + \Psi_{noise} \quad (4)$$

The atmospheric phase component, ψ_{atmo}, comprises two primary contributions: the ionospheric phase and the tropospheric phase. The tropospheric component is further divided into a stratified part and a turbulent part. The stratified phase is highly correlated with elevation, while ionospheric delays often exhibit large-scale spatial patterns that mimic orbital phase errors. To remove these large-scale trends, a 3D phase screen model is applied, defined as:

$$\Psi_{SIO} = ax + by + ch + z \quad (5)$$

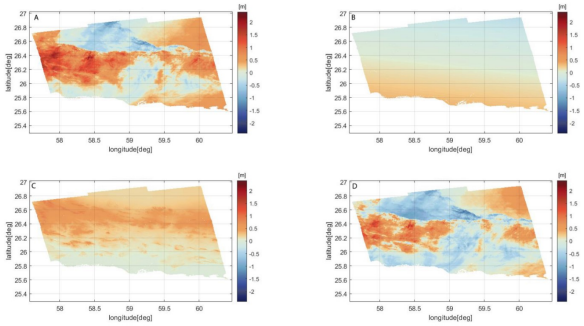

Figure 2. A: Interferometric Phase; B: Estimated Large-Scale Trend; C: Stratified Phase Component derived from the regional DEM; D: Residual Phase after removing trend and stratified effects.

Here, ψ_{SIO} represents the combined contribution of stratification, ionospheric artifacts, and orbital errors. Coefficients a and b capture orbital and ionospheric contributions, c models the stratified troposphere, and z is a reference offset. The variables x, y, and h represent the pixel's geographic coordinates and elevation.

This decomposition approach was systematically applied to all interferograms considered in this study. A representative result is illustrated in Figure 2.

To further investigate the tropospheric turbulent layer, various analytical techniques, such as power spectral density analysis, covariance evaluation, and variogram modeling, are commonly employed. In this study, we adopt the variogram function as the primary statistical tool to characterize turbulence. The analysis begins with the empirical estimation of directional variograms (east–west and north–south) to assess anisotropic behavior. Subsequently, a robust model is developed to quantify and interpret the observed turbulence patterns.

2.4 Empirical Variogram

Empirical variogram analysis of the turbulent atmospheric phase clearly demonstrates directional dependence when evaluated along north–south and east–west orientations (Figure 3). This directional variability signifies anisotropic behavior, reflecting that correlation structures differ depending on direction.

The empirical variogram results consistently exhibit directional features with varying degrees of anisotropy across different interferograms. The orientation and intensity of anisotropic patterns differ among individual frames. To systematically quantify these differences, empirical variograms are modeled explicitly incorporating anisotropic assumptions. Subsequently, anisotropy parameters, such as the direction and extent of anisotropy, are computed and analyzed across multiple datasets.

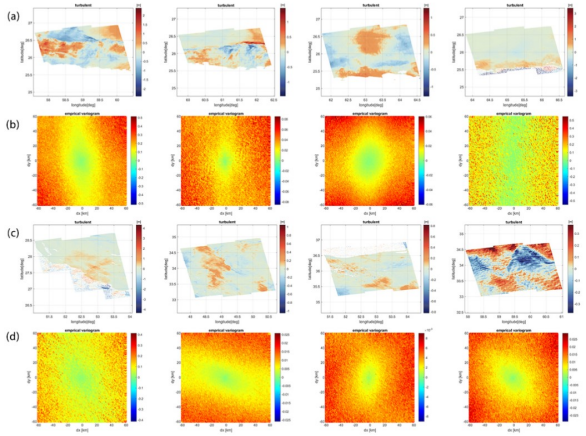

Figure 3. Rows (a) and (c) depict the tropospheric turbulent phase for coastal Makran and other study regions, respectively. Corresponding empirical variograms are shown in rows (b) and (d), illustrating clear directional variability.

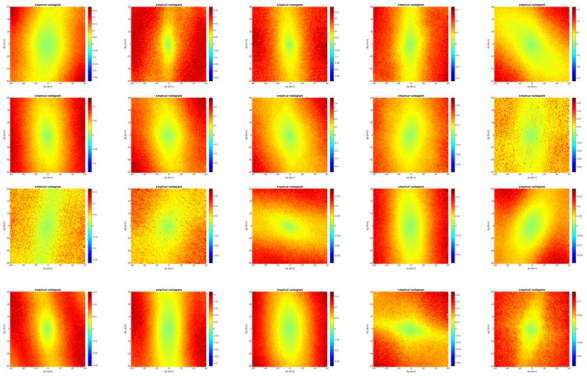

Figure 4. Twenty representative samples from the 1,200 computed empirical variograms (units: square meters), highlighting the directional dependence of tropospheric turbulence.

2.5 Modeling of Anisotropic Variograms

Determining the optimal variogram model to capture the behavior of empirical variograms is challenging. This study evaluates three standard variogram models, exponential, Gaussian, and spherical, to characterize the anisotropic structure of the tropospheric turbulent phase. Representative results for selected interferograms from the coastal Makran region are illustrated in Figure 5.

To objectively identify the most suitable model, we computed the root mean square error (RMSE) for each fit and selected the model with the lowest RMSE. Additionally, the isotropy ratio (IR) was introduced to quantify anisotropy, defined as:

$$IR = R_2/R_1 \quad (6)$$

Here, R_1 and R_2 represent the maximum and minimum correlation ranges derived from the modeled variograms. IR values range from 0 to 1, where values close to 1 indicate isotropy and values near 0 signify strong anisotropy.

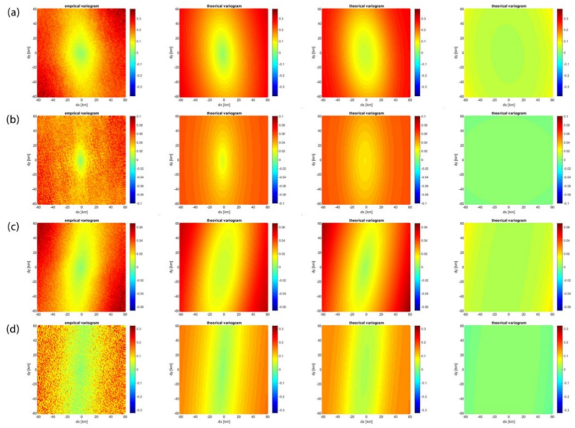

Figure 5. Empirical variograms modeled using exponential,- Gaussian, and spherical functions. Columns from left to right represent: empirical variogram, exponential model fit, Gaussian model fit, and spherical model fit, respectively. Data pertains to interferograms from the coastal Makran region.

The average RMSE across all interferograms for each modeling approach is presented in Figure 6, demonstrating the comparative effectiveness of each variogram type.

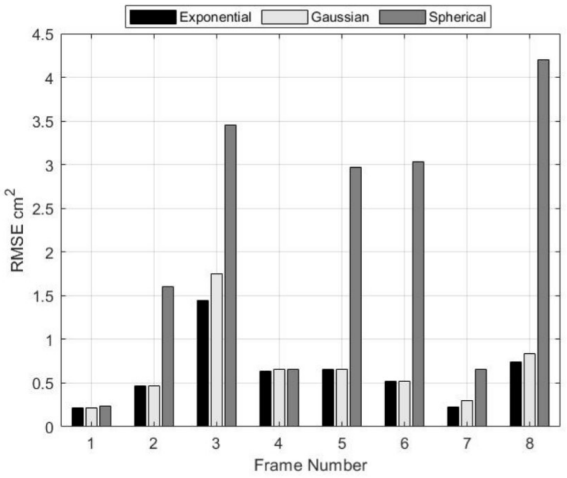

Figure 6. Average RMSE for variograms modeled using exponential (black), Gaussian (light gray), and spherical (dark gray) functions, calculated across 1200 interferograms.

Although the exponential and Gaussian functions produced similar outcomes, the exponential model consistently demonstrated superior performance across most interferograms, achieving reductions in RMSE by 55.62% and 4.10% compared to the spherical and Gaussian models, respectively (Tables 2 and 3).

To further analyze anisotropy, the average isotropy ratio for each frame was computed using the exponential model (Table 4). Coastal regions exhibited notably lower isotropy ratios, indicative of stronger anisotropic behavior. Detailed anisotropy distributions for the coastal Makran region are illustrated in Figure 8, highlighting differences relative to other study areas.

Overall, coastal areas display pronounced anisotropic patterns, likely influenced by moisture variability and complex topography, underscoring the importance of anisotropic modeling in these regions.

FN	Exponential	Gaussian	spherical
1	0.20	0.21	0.23
2	0.46	0.48	1.60
3	1.45	1.74	3.45
4	0.63	0.66	0.65
5	0.65	0.69	2.96
6	0.52	0.52	3.03
7	0.22	0.23	0.65
8	0.74	0.83	4.20

Table 2. The empirical variograms have been modeled in an anisotropic context using three approaches: exponential, Gaussian, and spherical. The root mean square error (RMSE) for each frame (FN: Frame Number) has been averaged. The exponential method consistently shows greater accuracy across all frames, exhibiting a lower RMSE compared to both the Gaussian and spherical methods.

FN	Impro(Exp/ Gau) %	Impro(Exp/Sph) %
1	4.76	13.04
2	4.16	71.25
3	16.66	57.97
4	4.54	3.07
5	5.79	78.04
6	0.28	82.70
7	4.34	66.15
8	10.84	82.38

Table 3. The exponential function demonstrates an average improvement of 55.62% compared to the spherical function and 4.10% compared to the Gaussian function.

Frame number	IR	Frame number	IR
1	0.6505	5	0.5063
2	0.7123	6	0.6009
3	0.6509	7	0.5812
4	0.5051	8	0.5012

Table 4. The isotropy ratio obtained from the exponential model has been averaged for each frame and is presented accordingly. Frames 1, 4, 5, 6, 7, and 8 represent coastal regions. It is observed that the intensity of anisotropy is more pronounced in these coastal frames, where values closer to zero indicate higher anisotropy and values closer to one indicate isotropy.

3. Refining Tropospheric Corrections via Anisotropic Assumptions

In this section, with the aim of evaluating and implementing the Least-Squares Collocation theory, the tropospheric delay signal is analyzed across two scenarios involving both coastal interferograms, under varying spatial scales and sampling strategies.

3.1 Scenario 1: Uniform and Sparse Sampling in a Coastal Region

In this scenario, interferograms from Frame 5 over the Makran coast were used to predict tropospheric delays under homogeneous sampling. Both isotropic and anisotropic models were tested.

The anisotropic model significantly outperformed the isotropic one, yielding a 19.6 cm improvement in delay correction accuracy, equivalent to a 40% gain.

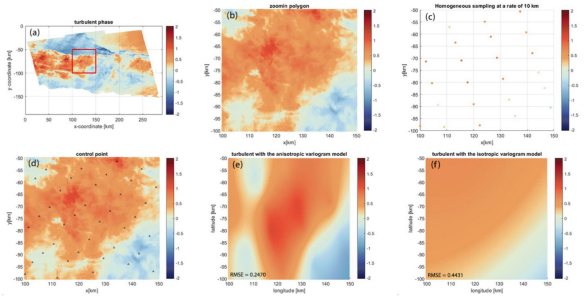

Figure 7. (a) Tropospheric turbulence phase and delineated study area; (b) magnified view of the selected region; (c) observation points at 10~km sampling intervals; (d) control points; (e) predicted tropospheric turbulence phase under the anisotropic model (RMSE shown, units in meters); (f) predicted tropospheric turbulence phase under the isotropic model (units in meters).

3.2 Scenario 2: Heterogeneous Sampling in a Coastal Region

In this scenario, another frame from the Makran coastal region was analyzed, with observational samples selected at low and uneven density.

Under these conditions, the anisotropic model achieved substantially higher accuracy in atmospheric delay correction, 15 cm better than the isotropic model, corresponding to a 50% improvement.

This study evaluated the impact of anisotropic assumptions on tropospheric delay correction across four distinct sampling scenarios involving both coastal and inland interferograms. Prediction experiments were performed using both isotropic and anisotropic models on 50 interferograms from the Makran coast, southern Zagros, and central Alborz regions.

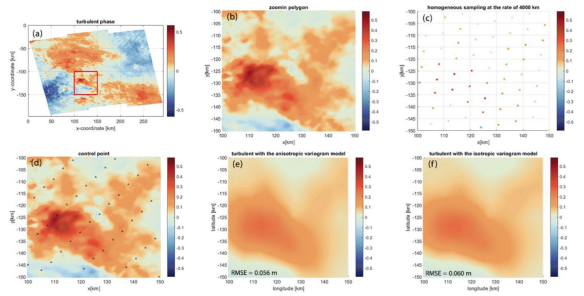

Figure 8. (a) Tropospheric turbulence phase and delineated region;(b) magnified view of the delineated area;(c) observation points with a sampling interval of 5~km;(d) control points;(e) predicted tropospheric turbulence phase under the anisotropic assumption; (f) predicted tropospheric turbulence phase under the isotropic assumption.

In all cases, the anisotropic model consistently outperformed the isotropic one. However, the extent of improvement depended strongly on the sampling configuration.

Under sparse or heterogeneous sampling, particularly in coastal regions, the anisotropic approach yielded significant improvements of up to 15 cm, or approximately 50%.

In contrast, for dense and uniform sampling, the performance difference was minimal, often below 0.5 cm. In such cases, the isotropic model may serve as a computationally efficient alternative with acceptable accuracy.

Therefore, it can be concluded that one of the key factors influencing the accuracy of tropospheric phase delay prediction in radar interferometry is the spatial density of observational samples. This insight is particularly valuable in InSAR applications such as land subsidence monitoring, earthquake deformation analysis, and infrastructure stability assessment, where the spatial distribution of observations can vary widely.

4. Conclusion and Recommendations

This study aimed to investigate the role of anisotropic assumptions in improving tropospheric delay corrections, particularly in coastal and non-coastal regions of Iran. Over 1,200 interferograms from six geodynamically and climatologically diverse areas, including western and eastern Makran, southern Zagros, central Alborz, and South Khorasan,were analyzed.

Using empirical variograms along east–west and north–south directions, significant anisotropic behavior was observed in all regions, especially in coastal areas. Anisotropic modeling using exponential variogram functions consistently outperformed isotropic approaches, achieving up to 56.8% lower RMSE in model fitting. The severity of anisotropy was strongly correlated with environmental moisture and proximity to the sea.

To evaluate the impact of anisotropy on actual delay correction, the Least-Squares Collocation method was implemented across four synthetic scenarios using both isotropic and anisotropic models. The results showed that:

- In sparse or heterogeneous sampling conditions, anisotropic modeling significantly improved correction accuracy, up to 15 cm or 50% improvement.
- In dense and uniform sampling scenarios, the difference was negligible, less than 0.5 cm, or around 2%.

Ultimately, anisotropy was found to be a critical factor in tropospheric delay correction, especially in low-density or anisotropically distributed datasets.

5. Recommendation

- Apply anisotropic modeling (particularly with exponential variogram functions) in subsidence monitoring and displacement estimation in regions with sparse observations or complex topography.
- In areas with isotropic geographic features and dense observations, isotropic assumptions may be sufficient and more computationally efficient.

This contribution has been peer-reviewed. The double-blind peer-review was conducted on the basis of the full paper.
https://doi.org/10.5194/isprs-annals-X-4-W8-2025-293-2026 | © Author(s) 2026. CC BY 4.0 License.

- Future studies are encouraged to incorporate meteorological models to validate and compare estimated delays against physically simulated atmospheric fields.

References

Agram, P., Simons, M., 2015. A noise model for InSAR time series. *Journal of Geophysical Research: Solid Earth*, 120(4), 2752–2771.

Fattahi, H., Amelung, F., 2015. InSAR bias and uncertainty due to the systematic and stochastic tropospheric delay. *Journal of Geophysical Research: Solid Earth*, 120(12), 8758–8773.

Ferretti, A., Prati, C., Rocca, F., 2001. Permanent scatterers in SAR interferometry. *IEEE Transactions on Geoscience and Remote Sensing*, 39(1), 8–20.

Gabriel, A. K., Goldstein, R. M., Zebker, H. A., 1989. Mapping small elevation changes over large areas: Differential radar interferometry. *Journal of Geophysical Research: Solid Earth*, 94(B7), 9183–9191.

Hanssen, R. F., 1998. Atmospheric heterogeneities in ERS tandem SAR interferometry. Delft University Press, Delft.

Hanssen, R. F., 2001. Radar interferometry: data interpretation and error analysis. Springer Science & Business Media.

Hu, F., Helfer, K. C., Siebesma, A. P., Hanssen, R. F., 2022. On the value of LES models for evaluating spatio-temporal tropospheric variability in multitemporal SAR interferograms. *IEEE Journal of Selected Topics in Applied Earth Observations and Remote Sensing*, 15, 7088–7099.

Jolivet, R., Grandin, R., Lasserre, C., Doin, M.-P., Peltzer, G., 2011. Systematic InSAR tropospheric phase delay corrections from global meteorological reanalysis data. *Geophysical Research Letters*, 38(17).

Jonsson, S., 2002. Modeling volcano and earthquake deformation from satellite radar interferometric observations. Stanford University.

Kinoshita, Y., Furuya, M., Hobiger, T., Ichikawa, R., 2013. Are numerical weather model outputs helpful to reduce tropospheric delay signals in InSAR data? *Journal of Geodesy*, 87, 267–277.

Knospe, S., Jonsson, S., 2009. Covariance estimation for dInSAR surface deformation measurements in the presence of anisotropic atmospheric noise. *IEEE Transactions on Geoscience and Remote Sensing*, 48(4), 2057–2065.

Li, Z., Duan, M., Cao, Y., Mu, M., He, X., Wei, J., 2022. Mitigation of time-series InSAR turbulent atmospheric phase noise: A review. *Geodesy and Geodynamics*, 13(2), 93–103.

Li, Z., Fielding, E., Cross, P., Preusker, R., 2009. Advanced InSAR atmospheric correction: MERIS/MODIS combination and stacked water vapour models. *International Journal of Remote Sensing*, 30(13), 3343–3363.

Löfgren, J. S., Björndahl, F., Moore, A. W., Webb, F. H., Fielding, E. J., Fishbein, E. F., 2010. Tropospheric correction for InSAR using interpolated ECMWF data and GPS zenith total delay from the Southern California Integrated GPS Network. *2010 IEEE International Geoscience and Remote Sensing Symposium*, IEEE, 4503–4506.

Massonnet, D., Feigl, K. L., 1995. Discrimination of geophysical phenomena in satellite radar interferograms. *Geophysical Research Letters*, 22(12), 1537–1540.

Massonnet, D., Feigl, K. L., 1998. Radar interferometry and its application to changes in the Earth's surface. *Reviews of Geophysics*, 36(4), 441–500.

Minh, D. H. T., Hanssen, R., Doin, M.-P., Pathier, E., 2022. Advanced Methods for Time-series InSAR.

Onn, F., Zebker, H., 2006. Correction for interferometric synthetic aperture radar atmospheric phase artifacts using time series of zenith wet delay observations from a GPS network. *Journal of Geophysical Research: Solid Earth*, 111(B9).

Sandwell, D. T., Price, E. J., 1998. Phase gradient approach to stacking interferograms. *Journal of Geophysical Research: Solid Earth*, 103(B12), 30183–30204.

Schmidt, D., Bürgmann, R., Nadeau, R., d'Alessio, M., 2005. Distribution of aseismic slip rate on the Hayward fault inferred from seismic and geodetic data. *Journal of Geophysical Research: Solid Earth*, 110(B8).

Wei, J., Li, Z., Hu, J., Feng, G., Duan, M., 2019. Anisotropy of atmospheric delay in InSAR and its effect on InSAR atmospheric correction. *Journal of Geodesy*, 93, 241–265.

Wei, M., Sandwell, D., Smith-Konter, B., 2010. Optimal combination of InSAR and GPS for measuring interseismic crustal deformation. *Advances in Space Research*, 46(2), 236–249.

Yu, C., Li, Z., Penna, N. T., Crippa, P., 2018. Generic atmospheric correction model for interferometric synthetic aperture radar observations. *Journal of Geophysical Research: Solid Earth*, 123(10), 9202–9222.

Zhan, W.-J., Li, Z.-W., Wei, J.-C., Zhu, J.-J., Wang, C.-C., 2015. A strategy for modeling and estimating atmospheric phase of SAR interferogram. *Chinese Journal of Geophysics*, 58(7), 2320–2329.